Supporting Information

Synergetic Evolution of Sacrificial Bonds and Strain-Induced Defects Facilitating Large Deformation of Bi_2Te_3 Semiconductor

Ben Huang,[†] Guodong Li,[*,‡,§] Bo Duan,[‡,§] Pengcheng Zhai[†,§] and William A. Goddard III[*,⊥]

[†]State Key Laboratory of Advanced Technology for Materials Synthesis and Processing, Wuhan University of Technology, Wuhan, 430070, China

[‡]Hubei Key Laboratory of Theory and Application of Advanced Materials Mechanics, Wuhan University of Technology, Wuhan, 430070, China

[§]Department of Engineering Structure and Mechanics, Wuhan University of Technology, Wuhan, 430070, China

[⊥]Materials and Process Simulation Center, California Institute of Technology, Pasadena, California 91125, United States

*William A. Goddard III. E-mail: wagoddard3@gmail.com
*Guodong Li. E-mail: guodonglee@whut.edu.cn

SI MD model and microstructure identification

The MD model of $(0001)\langle 1\bar{2}10\rangle$ slip system is shown in Figure S1. It is a cubic supercell with side length of 6 nm in a Cartesian representation. The Cartesian *z* axis is taken along [0001] crystallographic direction with the basal slip plane (0001) corresponding to *xy* plane, while Cartesian *y* axis coincides with the $[1\bar{2}10]$ direction. For PPP model, i.e. ideal crystal Bi_2Te_3, periodic boundary conditions are applied in all the three directions. For PSP model where there are two preset *xz* surfaces, free boundary conditions are adopted in *y* direction instead (Figure S1a).

After configuration relaxation, the crystal can achieve almost zero stress components (Figure S1b). Then the simulation of shear loading is implemented with one end fixed (e.g. fixed layers), while moving the loading layers with a constant velocity of 0.06Å/ps in the *y* direction. When discussing structural evolution during large deformation, the strain-induced defect particularly stacking fault (SF) should be well identified. As shown in Figure 2a in the manuscript, one had better study slip event or

partial dislocation in a cross section along $[0\bar{1}10]$ crystallographic direction. However, since all the models (including supercells and preset surfaces) are built in a Cartesian representation and the similar results can be shown in the section along *x* (rather than *y*) direction, microstructure identification in *xz* cross section is preferable here for the convenience of discussion (Figure S2).

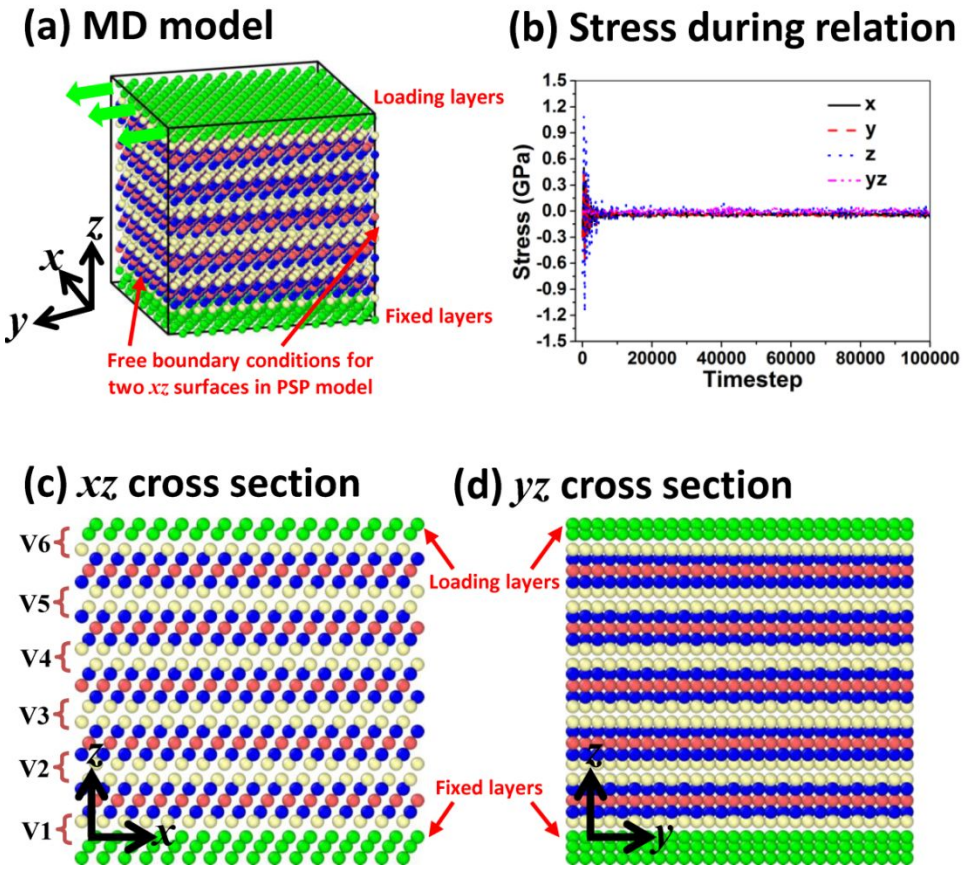

Figure. S1 Schematic of the MD model of Bi_2Te_3 crystal under shear loads. (a) The boundary conditions and loading approach in simulation. (b) The stress-strain relationships during configuration relaxation. The initial configuration with fixed and loading layers in (c) *xz* and (d) *yz* cross section.

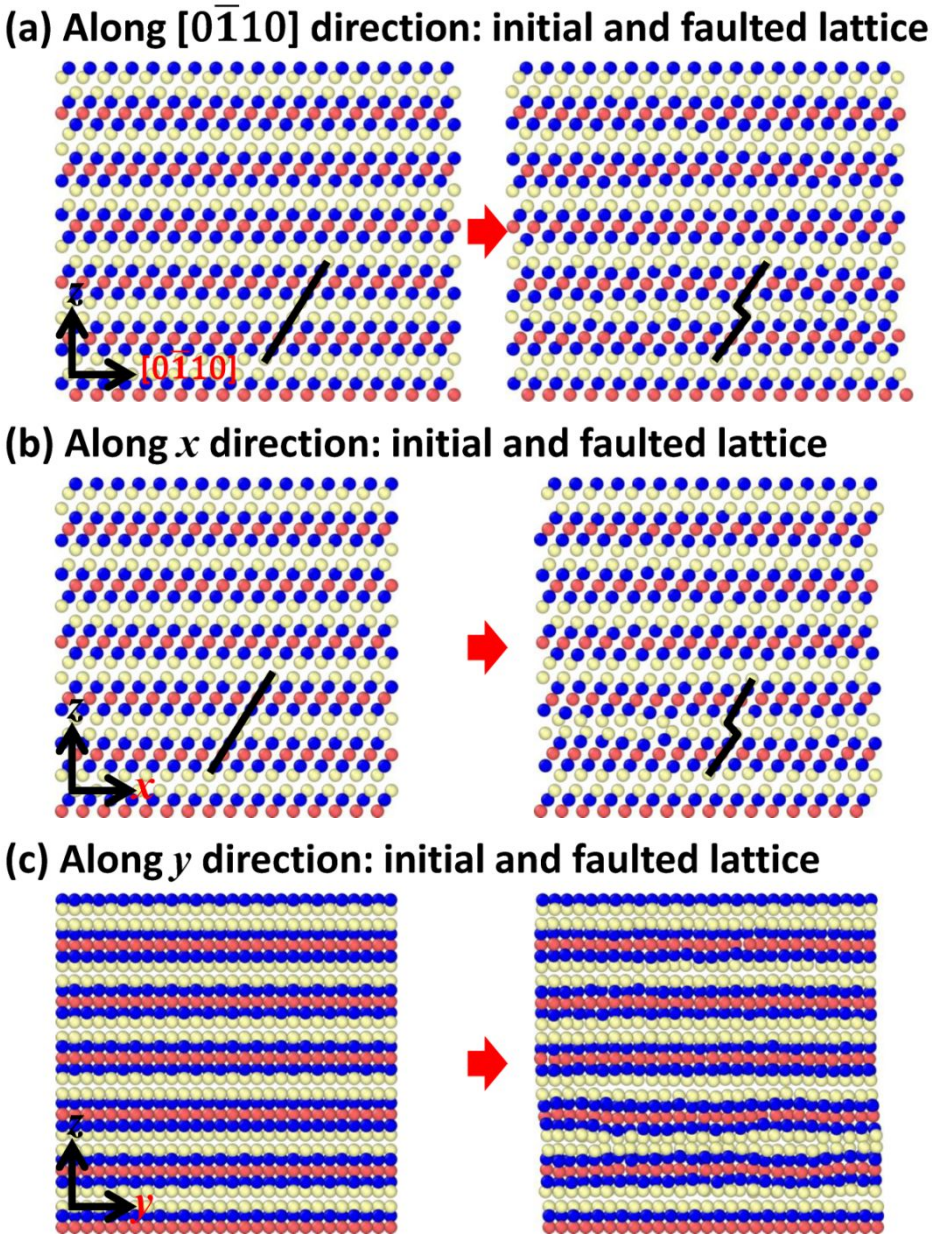

Figure. S2 The initial and faulted lattice during shear deformation displayed in the cross section along (a) $[0\bar{1}10]$ crystallographic direction, (b) *x* Cartesian direction and (c) *y* Cartesian direction.

SII Size effects of Bi_2Te_3 crystal

As the abstraction of ideal Bi_2Te_3 crystal, PPP models with side length of 6, 9 and 15 nm share the similar mechanical behavior during shearing, namely the sophisticated evolution of local structures demonstrated in Figure 1 and 2 in the manuscript. And we highlight that all these local deformation between Te1-Te1 layers are homogeneous, which can be also confirmed by the fracture configurations

of the two large models in Figure S3. However, in large PPP models, the peaks in stress-strain curves tend to be irregular (Figure S3a), since several slip planes may be enabled almost simultaneously in different Te1-Te1 layers and thereby one peak usually measures a stress release for multiple slips at large strain. "Solo slip per peak" is undoubtedly preferred for the observation and analysis in this work, which can be more easily realized by a small PPP model under proper conditions (e.g. a requirement for the simulation setup).

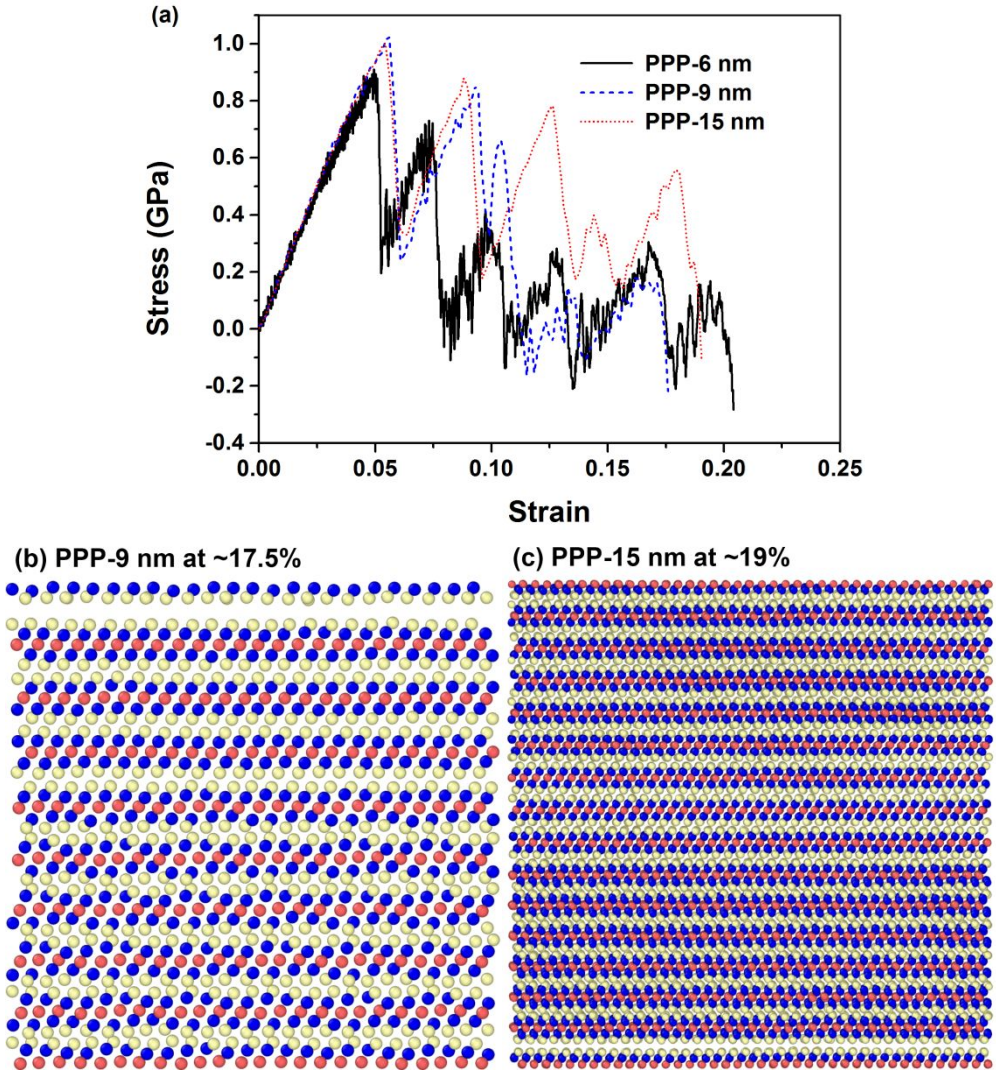

Figure. S3 Deformation behavior of ideal crystal Bi_2Te_3 with different model sizes. (a) The stress-strain relationships of PPP models with side length of 6, 9 and 15 nm. (b) The fracture structure of PPP-9 nm model at 0.175 strain. (c) The fracture structure of PPP-15 nm model at 0.19 strain.

For inorganic solid materials, it has been reported that achieving small crystal size will probably

improve mechanical performance such as strength and ductility.[1-5] Here we show this size effect can also tune the homogeneity of local deformation in Bi_2Te_3. Given surface is a lattice defect or disorder, the load response of the atoms on and near surfaces should be perturbed compared with that of the intact interior regions.[6, 7] In Bi_2Te_3 crystals with larger sizes (e.g. PSP-9 and 15 nm models), this difference between surface and interior appears more distinct, likely leading to heterogeneous deformation between Te1-Te1 layers under the same load condition (Figure S4). Besides suppressing subsequent slips, it will induce more disorder (e.g. micro-cracks or SF/strengthening of only a part of atoms/bonds) that is difficult to be completely recovered despite the self-healing nature of VdW during shearing (Figure S4b-c). Therefore in the further distorted Bi_2Te_3 lattice, the shear stress gradually decreases after the first peak, and meanwhile this lattice tends to fracture with lower strain (Figure S4a), indicating a cumulative disadvantage of mechanical degradation. However, it should also be pointed out that smaller Bi_2Te_3 nanocrystals may be induced by shear strain (e.g. cleavage on Te1 layers), which is usually desired for high-performance TE materials in turn.[8-10]

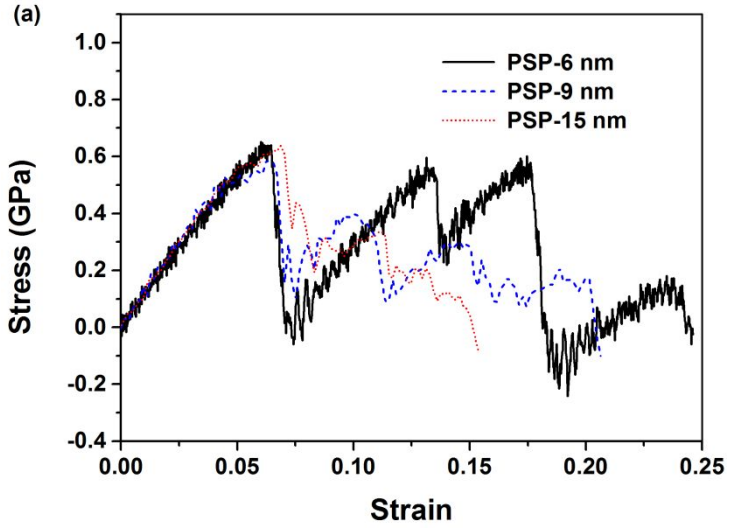

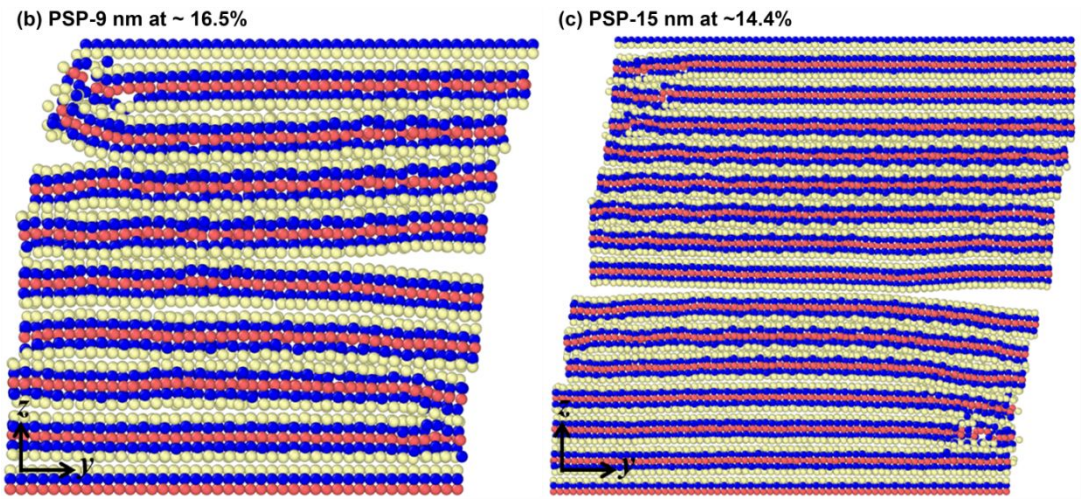

Figure. S4 Deformation behavior of nanocrystal Bi_2Te_3 with different model sizes. (a) The stress-strain relationships of PSP models with side length of 6, 9 and 15 nm. (b) The nonuniformly distorted structure of PSP-9 nm model at 0.165 strain. (c) The nonuniformly distorted structure of PSP-15 nm model at 0.144 strain. The configurations here are displayed in *yz* plane.

On the other hand, in a very small nanocrystal (e.g. PSP-6 nm model) with high surface-to-volume ratio, there will be not only significant surface effects but also high affected-bonds-to-all ratio, which can be regarded as bond engineering via planar defects. Hence compared with large crystals, the difference of structural evolution during shearing between surface and interior will probably get slighter and smoother to facilitate homogeneous deformation of a whole Te1 layer. In this much less distorted lattice, more slip planes may be enabled to bear larger strain and meanwhile more VdWs work as SB. Considering the intensified interaction between SB and defect in nanostructures to spontaneously maintain/recover the lattice order (e.g. enhanced ability of order protection, see Figure S4a; also Figure 3 and 4 in the manuscript), it partly reveals the role of ultrafine grains (e.g. 5-20 nm) on the mechanical improvement of high-performance Bi_2Te_3 materials.[11-13] But it is still an open question of the size effects on Bi_2Te_3 mechanical performance, because too small crystals (e.g. less than 5 nm) have much distorted initial configurations compared with the ideal crystal, which may also results in heterogeneous deformation under loads. Besides, our previous tensile simulations of Bi_2Te_3 nanofilms with thickness of 3-15 nm show size-dependent elastic moduli from 37.2 to 53 GPa,[6] while at the sizes of ultrafine nanocrystals here, the three PSP models share a similar shear modulus of about 12 GPa without such a distinct difference. Thus for much larger models (e.g. coarse grains), further study on this size effect of

bond weakening is still necessary.

SIII Surface effects on Bi_2Te_3 slips

This part will discuss the dislocation-mediated deformability of Bi_2Te_3 crystal tuned by surfaces in different directions. In accord with the simulation in the manuscript, $(0001)\langle 0\bar{1}10\rangle$ and $(0001)\langle 1\bar{2}10\rangle$ slip systems are considered through cubic models with side length of 6 nm and shear loading is implemented by moving the specified layers in the *y* direction, while surfaces are preset in *x*, *y, z* and all direction, respectively (e.g. SPP, PSP, PPS and SSS model). Given the evolution of Bi_2Te_3 HBS is primarily dominated by the bond response of VdW between Te1 layers and meanwhile the slidable Te1 atoms share the similar trajectory that has found to be always along $[0\bar{1}10]$ or $[1\bar{1}00]$ Burgers (Figure 1 and 2 in the manuscript), the critical shear stress can measure the ease of basal slip on Te1 layers of each system (Figure S5).

(1) $(0001)\langle 0\bar{1}10\rangle$ system

As stated in the manuscript (Figure 1b and 2a), slip will most likely occur in this system for the same direction of Te1 atomic trajectory and applied load. In SPP or PPS model, VdW in this trajectory on a specific basal plane is only little affected by the preset surfaces compared with that of PPP model (e.g. ideal crystal), leading to the almost unchanged shear modulus and critical stress of 18 and 0.6 GPa. By contrast, PSP model has the lowest shear modulus and critical stress of 9.3 and 0.35 GPa that is close to the SSS one and easiest to shear, because partial dislocations form in $[0\bar{1}10]$ Burgers that is perpendicular to the surface with the most broken bonds due to the loss of neighboring atoms. It is indicated that the shear deformability of Bi_2Te_3 crystal directly relates to VdWs that indeed bear the applied load in practice, which can be found in other slip systems similarly.

(2) $(0001)\langle 1\bar{2}10\rangle$ system

In this case, the applied load is taken along $[1\bar{2}10]$ direction of Bi_2Te_3 crystal (e.g. also Cartesian *y* axis), while the Te1 trajectory is still in $[0\bar{1}10]$ Burgers. The *x* displacement component of this trajectory results in some differences in stress-strain curves such as a larger critical stress in PPP and PPS compared with that of $(0001)\langle 0\bar{1}10\rangle$ system (e.g. 0.9 versus 0.6 GPa at about 0.05 strain, see Table S1 for detail). For the quite few VdWs to resist shear deformation, PSP model still exhibits very

low shear modulus and critical stress of 11.9 and 0.65 GPa inferior to that of SSS one (e.g. 9.9 and 0.48 GPa). It is concluded that a slip system of Bi_2Te_3 nanocrystal can be more easily enabled via surfaces laid in the slidable trajectory. Besides, Figure S5 shows that the mechanical stability and failure strain during shearing, which relates to the present order of distorted lattice, can be affected by surfaces in different lattice directions as defect or nanostructure engineering (also Figure 3 and 4 in the manuscript). And considering the enhanced ability to hold the integrity and order of Bi_2Te_3 crystal that can intuitively demonstrate the synergetic evolution of SB and defect, we mainly focus on the deformability tuning of this PSP model along $(0001)\langle 1\bar{2}10\rangle$ system in the manuscript. In addition, there may be a small and temporary negative stress in the related stress redistribution during each slipping due to the dramatic structural changes. However, since surface effects can promote smoother structural evolution particularly during a continuous slippage, it is no surprise that the whole deformation process of PSP model roughly exhibits less significant stress release compared with PPP one.

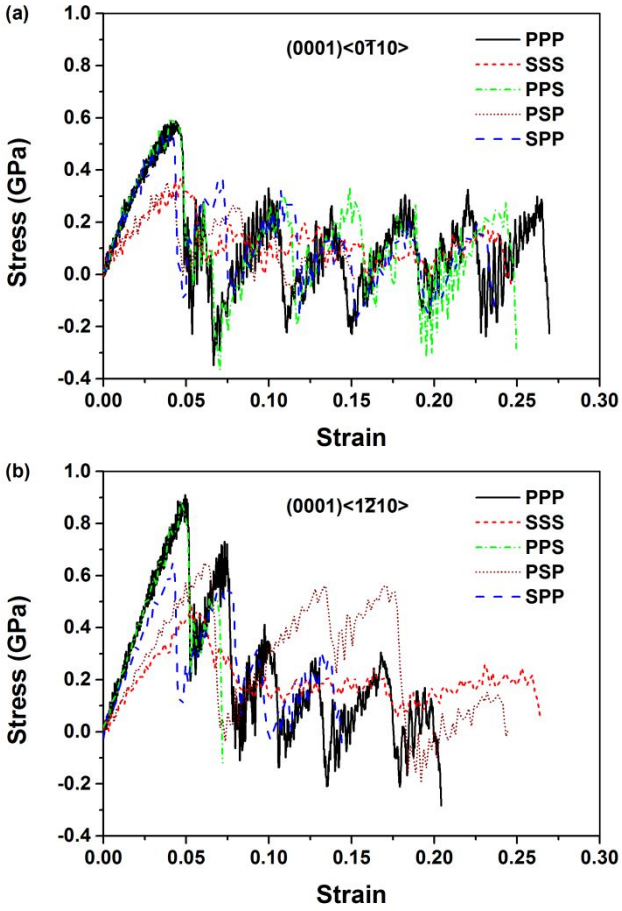

Figure. S5 The stress-strain relationships of nanocrystal Bi_2Te_3 with surfaces in different

directions: (a) $(0001)\langle 0\bar{1}10\rangle$ system, and (b) $(0001)\langle 1\bar{2}10\rangle$ system.

Table S1. The predicted critical shear stress τ_c and shear modulus C_{44} (in GPa).

	PPP	SSS	PPS	PSP	SPP
τ_c-$(0001)\langle 0\bar{1}10\rangle$	0.6	0.37	0.6	0.35	0.56
τ_c-$(0001)\langle 1\bar{2}10\rangle$	0.9	0.48	0.9	0.65	0.65
C_{44}-$(0001)\langle 0\bar{1}10\rangle$	18	9.5	18.6	9.3	18
C_{44}-$(0001)\langle 1\bar{2}10\rangle$	18.6	9.9	18.6	11.9	17

SIV Alternating slips in Bi_2Te_3 nanocrystal

This part will illuminate the alternating events of basal slips in PSP model along $(0001)\langle 1\bar{2}10\rangle$ system. After the continuous slippage at 0.067 strain on Te1 layers labeled as "V4", the increasing strain will enable slip plane alternately on different Te1 layers, i.e. V3 at 0.14, V4 and V5 at 0.185, and V2 and V6 at 0.25. The slip on V6 results in a cleavage (CL) to fracture the nanocrastal, and this ultimate configuration at 0.25 strain is shown in Figure S6. Moreover, during the following slips over 0.067 strain, all SFs occur with VdW strengthening. For example, around 0.185 strain V4 Te1 layers (or around 0.14 strain V3 layers) undergo a significant energy reduction over 82 eV, which can be identified as the local reinforce of Bi_2Te_3 HBS with VdW contraction (Figure 3 in the manuscript). Therefore these planar defects are stable and less deformable on the same load condition, leaving behind as LPD found in the ultimate configuration.

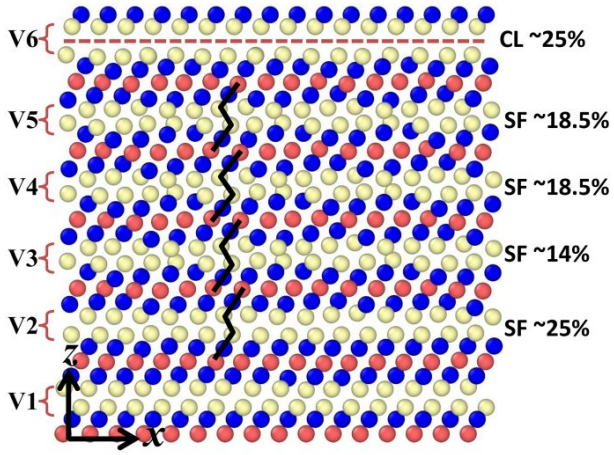

Figure. S6 The fracture structure at 0.25 strain with a history of local plastic deformations (LPD).

SV Unloading process of ideal crystal Bi_2Te_3

As the supplemental information, the comparative results of unloading process of ideal crystal are given here to in turn highlight the surface effects of ultrafine grains on the stability of SF and thereby the reversibility of local deformation (Figure S8; also Figure 3 and 4 in the manuscript). When shear load is applied to PPP model, a slip occurs at about 0.053 strain to form SF of Te1 layers labeled as "V2" (Figure S7c) while VdWs between these layers are contracted and strengthened, which can be measured by a reduction of lattice energy over 82 eV (Figure 1 and 2 in the manuscript). In this case, the model is unloaded at 0.06 strain (e.g. just after slipping) to show an irreversible deformation. For tiny change of the atomic configuration and related energy during unloading in V2 (Figure S7b-c), it is clearly a stable SF that can remain as LPD after this unload process. And two "selective" slips alternately occur in V4 and V3 at 0.01 and 0.044 unload strain to dissipate energy and release stress, resulting in new stable SFs in the distorting lattice and the asymmetry of stress-strain curve (Figure S7a and c).

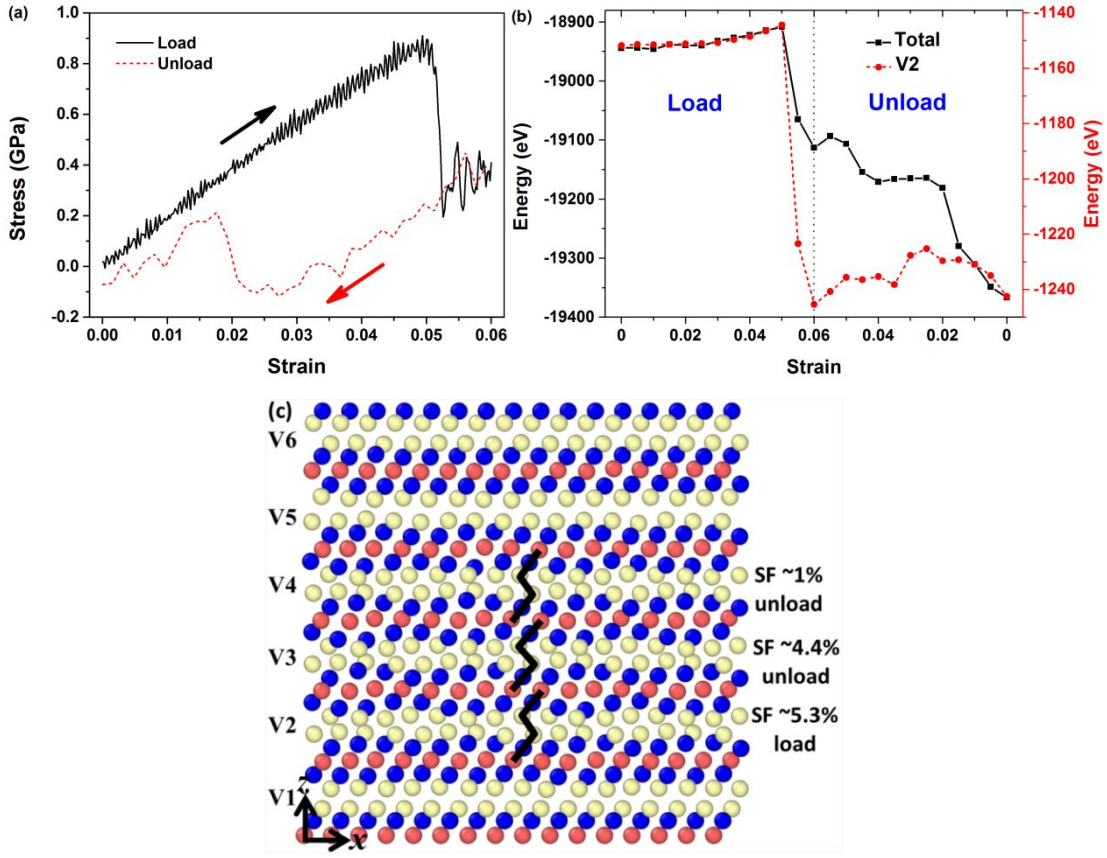

Figure S7 Unload behavior of ideal crystal Bi_2Te_3 along $(0001)\langle 1\bar{2}10\rangle$ system. (a) The stress-strain relationships in loading and unloading process. (b) The related energy of the whole lattice

and the faulted Te1 layers. (c) The ultimate structure after unload strain 0.06 with a history of local plastic deformations.

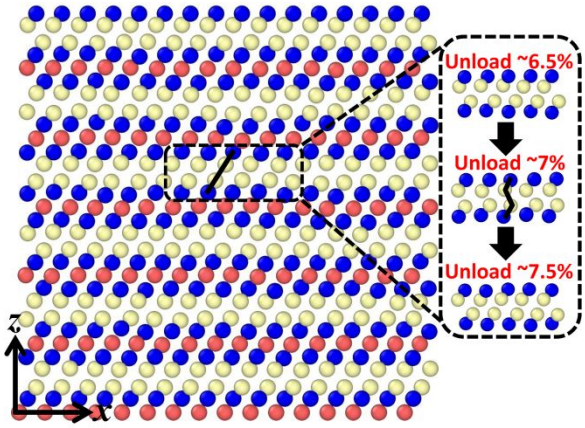

Figure S8 Unload behavior of nanocrystal Bi_2Te_3 along $(0001)\langle 1\bar{2}10\rangle$ system with surfaces normal to $[1\bar{2}10]$ direction. The ultimate structure after unload strain 0.08 with the evolution history of an unstable stacking fault (SF), which is compared with Figure S7c.

References

(1) Youssef, K. M.; Scattergood, R. O.; Murty, K. L.; Horton, J. A.; Koch, C. C., Ultrahigh strength and high ductility of bulk nanocrystalline copper. *Appl. Phys. Lett.* **2005,** 87, (9), 091904.

(2) Wu, B.; Heidelberg, A.; Boland, J. J., Mechanical properties of ultrahigh-strength gold nanowires. *Nature Materials* **2005,** 4, (7), 525-529.

(3) Yu, Q.; Qi, L.; Mishra, R. K.; Li, J.; Minor, A. M., Reducing deformation anisotropy to achieve ultrahigh strength and ductility in Mg at the nanoscale. *Proc. Natl. Acad. Sci.* **2013,** 110, (33), 13289-13293.

(4) Liu, B.-Y.; Liu, F.; Yang, N.; Zhai, X.-B.; Zhang, L.; Yang, Y.; Li, B.; Li, J.; Ma, E.; Nie, J.-F.; Shan, Z.-W., Large plasticity in magnesium mediated by pyramidal dislocations. *Science* **2019,** 365, (6448), 73-75.

(5) Schiøtz, J.; Di Tolla, F. D.; Jacobsen, K. W., Softening of nanocrystalline metals at very small grain sizes. *Nature* **1998,** 391, 561.

(6) Tong, Y.; Yi, F.; Liu, L.; Zhai, P.; Zhang, Q., Molecular dynamics study of mechanical properties of bismuth telluride nanofilm. *Physica B* **2010,** 405, (15), 3190-3194.

(7) Tong, Y.; Yi, F. J.; Liu, L. S.; Zhang, Q. J., Molecular dynamics simulation of mechanical properties of single-crystal bismuth telluride nanowire. *J. Electron. Mater.* **2010,** 39, (9), 1730-1734.

(8) Zhai, P. C.; Zhao, W. Y.; Li, Y.; Liu, L. S.; Tang, X. F.; Zhang, Q. J.; Niino, M., Nanostructures and enhanced thermoelectric properties in Ce-filled skutterudite bulk materials. *Applied Physics Letters* **2006,** 89, (5), 052111.

(9) Rogl, G.; Grytsiv, A.; Rogl, P.; Royanian, E.; Bauer, E.; Horky, J.; Setman, D.; Schafler, E.; Zehetbauer, M., Dependence of thermoelectric behaviour on severe plastic deformation parameters: A case study on p-type skutterudite DD0.60Fe3CoSb12. *Acta Materialia* **2013,** 61, (18), 6778-6789.

(10) Hussain, N.; Zhang, Q.; Lang, J.; Zhang, R.; Muhammad, M.; Huang, K.; Cosseron De Villenoisy, T.; Ya, H.; Karim, A.; Wu, H., Ultrahigh Room-Temperature Photoluminescence from Few to Single Quintuple Layer Bi2Te3 Nanosheets. *Advanced Optical Materials* **2018,** 6, (13), 1701322.

(11) Xie, W.; Tang, X.; Yan, Y.; Zhang, Q.; Tritt, T. M., Unique nanostructures and enhanced thermoelectric performance of melt-spun BiSbTe alloys. *Appl. Phys. Lett.* **2009,** 94, (10), 102111.
(12) Shen, J. J.; Zhu, T. J.; Zhao, X. B.; Zhang, S. N.; Yang, S. H.; Yin, Z. Z., Recrystallization induced in situ nanostructures in bulk bismuth antimony tellurides: a simple top down route and improved thermoelectric properties. *Energ. Environ. Sci.* **2010,** 3, (10), 1519-1523.
(13) Poudel, B.; Hao, Q.; Ma, Y.; Lan, Y.; Minnich, A.; Yu, B.; Yan, X.; Wang, D.; Muto, A.; Vashaee, D.; Chen, X.; Liu, J.; Dresselhaus, M. S.; Chen, G.; Ren, Z., High-thermoelectric performance of nanostructured bismuth antimony telluride bulk alloys. *Science* **2008,** 320, (5876), 634-638.